# Supporting Information

## Synchronizing Crystallization Enables Thermally Stable All-FA Pb-Sn Perovskites for Printable MA-Free All-Perovskite Tandem Solar Cells

*Hongbing Li[1], Wei Feng[2], Jianan Wei[2], Qingchen He[1], Haojiang Shen[3], Yi He[4], Shi Chen[3*], Yang Hao[4], Christoph J. Brabec[5], Yaohua Mai[1,6*], Fei Guo[1*]*

[1]Institute of New Energy Technology, College of Physics and Optoelectronic Engineering, Jinan University, Guangzhou, 510632, China

[2]College of Information Science and Technology, Jinan University, Guangzhou, 510632, China

[3]Henan Key Laboratory of Quantum Materials and Quantum Energy, School of Future Technology, Henan University, Zhengzhou, 450046, China

[4]College of Physics and Optoelectronics, Key Lab of Advanced Transducers and Intelligent Control System, Taiyuan University of Technology, Taiyuan, 030024 China

[5] Institute of Materials for Electronics and Energy Technology (i-MEET), Department of Materials Science and Engineering, Friedrich-Alexander-Universität (FAU) Erlangen-Nürnberg, Martensstraße 7, 91058 Erlangen, Germany.

[6]Guangdong Mellow Energy Co., Ltd., Guangzhou, 510630, People's Republic of China

*Correspondence: S. C. (chenshi@henu.edu.cn); Y. M. (yaohuamai@jnu.edu.cn); F. G. (fei.guo@jnu.edu.cn)

## Experimental Section

### Material and Reagent:

All chemicals were purchased from commercial suppliers and used as received unless otherwise specified. Lead iodide ($PbI_2$, 99.985%), Lead bromide ($PbBr_2$, 99.999%), Cesium Iodide (CsI, 99.999%), PEDOT:PSS (Heraeus-Clevios 4083), poly[bis(4-phenyl)(2,4,6-trimethylphenyl)amine] (PTAA), phenethylammonium bromide (PEABr, >99.5%) and 1,3-Propanediamine hydroiodide (PDADI, ≥99.5%) were purchased from Xi'an Polymer Light Technology. [4-(3,6-Dimethyl-9H-carbazol-9-yl) butyl] phosphonic acid (Me-4PACz, >99.0%), Nickel oxide (NiOX, 99.9%) nanoparticles, fullerene ($C_{60}$, 99.9%) and Methyl[6,6]-phenyl-$C_{61}$-butyrate ($PC_{61}BM$, 99.5%) were purchased from Shanghai Weizhu Chemical Technology Co., Ltd. Formamidinium iodide (FAI) were purchased from Greatcell Solar Materials Pty Ltd. Tin(II) iodide ($SnI_2$, 99.99%) was purchased from Advanced Election Technology CO,.Ltd. Tin(II) fluoride ($SnF_2$) and all solvents were purchased from Sigma-Aldrich. Hydrazinium dichloride (HDC) was purchased from Macklin. Tetrakis (dimethylamino) tin (IV) (99.999%) was purchased from Shanghai Yuanxiang Chemical Co., LTD. The glass ITO with a sheet resistance of ~16 ohm/sq were purchased from Yingkou OPV. Ag was purchased from Sante Materials Co., LTD.

### Blade Deposition of Sn-Pb Perovskite Films:

The 1.8 M $MAPbI_3$ precursor solution was prepared by dissolving 829.9 mg $PbI_2$ and 286.2 mg MAI in a mixed solvent of 800 μL DMF and 200 μL DMSO. The 1.8 M $MASnI_3$ precursor solution was prepared by dissolving 669.6 mg $SnI_2$ and 286.2 mg

MAI with 10 mol% (28.1 mg) $SnF_2$ in a mixed solvent of 800 μL DMF and 200 μL DMSO. The 1.8 M $FAPbI_3$ precursor solution was prepared by dissolving 829.9 mg $PbI_2$ and 309.6 mg FAI in a mixed solvent of 800 μL DMF and 200 μL DMSO. The 1.8 M $FASnI_3$ precursor solution was prepared by dissolution of 669.6 mg $SnI_2$ and 309.6 mg FAI with 10 mol% (28.1 mg) $SnF_2$ in a mixed solvent of 800 μL DMF and 200 μL DMSO. The $(MAPbI_3)_{0.5}(MASnI_3)_{0.5}$ perovskite precursor solution was obtained by mixing the $MAPbI_3$ and $MASnI_3$ stock solutions with a volume ratio of 5:5. The $(MAPbI_3)_{0.5}(FASnI_3)_{0.5}$ perovskite precursor solution was obtained by mixing the $MAPbI_3$ and $FASnI_3$ stock solutions with a volume ratio of 5:5. The $(FAPbI_3)_{0.5}(FASnI_3)_{0.5}$ perovskite precursor solution was obtained by mixing the $FAPbI_3$ and $FASnI_3$ stock solutions with a volume ratio of 5:5. The $FA_{0.8}Cs_{0.2}Pb_{0.5}Sn_{0.5}I_3$ perovskite precursor solution was prepared by dissolving 415 mg $PbI_2$, 335 mg $SnI_2$, 247.6 mg FAI and 93.6 mg CsI with 10 mol% (14.1 mg) $SnF_2$ in a mixed solvent of 800 μL DMF and 200 μL DMSO. And the HDC-processed all-FA based Pb-Sn mixed perovskite precursor solution were prepared by adding different amount of HDC (1, 2.5, 4 mg) into the $(FAPbI_3)_{0.5}(FASnI_3)_{0.5}$ solution. Blade coating of the perovskite precursor films was carried out on a commercial blade coater (PRINEQU® from HUITUOPTOELECT Co.Ltd, Guangzhou) at room temperature in nitrogen-filled glovebox. The gap for solution load between the substrate (25 × 25 mm) and blade was fixed at 200 μm and the coating speed was fixed at 7 mm/s. Once the precursor solution spread onto the substrate by blade-coating, the liquid precursor film was transferred to the transfer chamber of glove box, which was pumped down to the

lower limit of the pressure gauge (-0.1 MPa relative to atmospheric pressure, i.e., ~1000 Pa) within 15 s using an Edwards RV12 pump and maintained under continuous pumping for 90 s. Subsequently, the films were taken out of the transfer chamber and annealed at 160 °C for 2 minutes and 100 °C for 8 minutes.

**Fabrication of all-FA Pb-Sn perovskite solar cells**:

For a small-area device, the prepatterned ITO-coated glass (OPV Tech Co., Ltd.) was sequentially cleaned by sonicating the substrates in glass water, deionized water and ethanol for 15 min each. The hole transporting layer was spin-coated from mixed solvent of deionized water and PEDOT:PSS stock solution (volume ratio 3:1) at 4000 rpm for 30 s and the film was then annealed at 150 °C for 10 min in ambient air. The substrate was transferred to a nitrogen-filled glovebox after it cooled down to room temperature. The perovskite absorber layer was subsequently deposited using the vacuum-assisted blade-coating method as described above. To realize surface passivation, a solution of PEABr with different concentration (1, 2, 3 mg/mL) in isopropanol was spin-coated on top of the HDC-processed perovskite films. The prepared perovskite thin films further dried at 100 °C for 10 min inside the glovebox. Subsequently, electro-transporting layer $PC_{61}BM$ (4 mg/mL in chlorobenzene) was successively deposited on top of perovskite films by spin coating at 5000 rpm for 30 s. Then, the substrates were transferred to the evaporation system and a 20 nm thick C60 was evaporated. After that, the substrates were then transferred to the ALD system (TALD-200, KE-MICRO Co., Ltd) to deposit ~15 nm $SnO_2$ at 80° C using precursors of tetrakis (dimethylamino) tin (IV) and deionized water. Finally, 100 nm Ag electrode

were evaporated on ALD-$SnO_2$ layer. The active area of the solar cells was 0.09 $cm^2$, which is determined by the overlapping between the top Ag and bottom ITO electrode.

For the 5 × 5 $cm^2$ modules, the first pattering step (P1), the 5*5 $cm^2$ ITO-coated glass are patterned with a nanosecond infrared laser (1064 nm) in order to disconnect the bottom electrode and define the cell dimensions. In the second patterning step (P2), the interconnection between neighboring cells is formed by a selective removal (see in **Figure 3d**) of all layers atop the ITO bottom electrode: PEDOT:PSS, perovskite, PEABr, PCBM, C60 and ALD-$SnO_2$ layers. P2 patterning is achieved using a nanosecond green laser (532 nm). The devices are completed with the third patterning step (P3), which disconnects the top electrode by thermal evaporation of Ag on a prepatterned mask.

**Fabrication of MA-free all-perovskite tandem solar cells**:

ITO substrates were cleaned as described above. Then, $NiO_x$ aqueous solution (10 mg $mL^{-1}$) was spin-coated onto the ITO substrates at 3000 rpm for 30 s and annealed on a hotplate at 130°C for 10 min in air. After cooling, the substrates were immediately transferred to an $N_2$-filled glovebox. Then, the self-assembled monolayers (SAM) of Me-4PACz (0.5 mg $mL^{-1}$) in IPA without doping was spin-coated on the $NiO_x$ film at 5000 rpm for 30 s and was then annealed at 150 °C for 10 min. The wide-bandgap perovskite ($FA_{0.8}Cs_{0.2}Pb(I_{0.6}Br_{0.4})_3$ ~1.77 eV) film was deposited on top of SAM-modified-$NiO_x$ with the vacuum assisted blade coating method. The precursor solution was prepared by dissolving 0.28 mmol CsI, 1.12 mmol FAI, 0.56 mmol $PbI_2$ and 0.84 mmol $PbBr_2$ into 1 mL of mixed solvents (DMF:DMSO = 4:1 by volume). The

gap for solution load between was fixed at 200 μm and the coating speed was fixed at 5 mm/s. Immediately after the blade coating was completed, the freshly coated liquid precursor film was transferred to a vacuum chamber, which was pumped to 1000 Pa within 10 s and stayed at that pressure for 90 s. Subsequently, the substrates were then transferred onto a hotplate and heated at 100°C for 10 min. After cooling to room temperature, a 20-nm-thick C60 film and a 20 nm-thick ALD-$SnO_2$ were subsequently deposited on top by thermal evaporation and ALD. Then, a-5nm-thick Au was deposited on the layer of ALD-$SnO_2$. After this, PEDOT:PSS solution (dispersed in isopropanol) was spin-coated on the substrates at 3500 rpm for 30s and annealed at 120°C for 10 min in ambient air. The subsequent fabrication steps followed the same procedures as those used for the optimal single-junction all-FA Pb-Sn perovskite solar cells, leading to the completion of the monolithic tandem solar cells.

**Characterizations**:

In-situ PL setup (PeroTrack-520, Light Physics Electro-Optics Technology (Shenzhen) Co., Ltd) consist of a vacuum chamber, laser, fiber optic prob, and pressure control system. The perovskite wet film, blade-coated on glass, is placed inside the vacuum chamber at an angle of 45°. A 520 nm laser serves as the excitation source, illuminating the film through a transparent window. The PL signal emitted from the film is collected by a fiber optic probe positioned at an angle to minimize reflection interference, and the signal is then transmitted to an external spectrometer for real-time analysis. The pressure control system is designed to regulate the vacuum chamber's pressure. Initially, the system reduces the pressure to 13.25 Mbar within the first 15

seconds, maintaining this pressure until the 95-second mark. Afterward, the chamber is gradually refilled with $N_2$ to restore the pressure. The sample remains inside the vacuum chamber until the 180-second mark.

The crystal structure was characterized by Bruker D8 Advance X-ray diffractometer with CuKα radiation operated at 40 kV and 40 mA. The Sn element of Pb-Sn mixed perovskite films was measured using XPS (AXIS ULTRA DLD, aluminum Kα X-ray radiation, Kratos Analytical Ltd.). The UV-vis absorption was measured by a double-beam spectrophotometer (Lambda 950, PerkinElmer) equipped with an integrated sphere. The surface morphology of the thin films and devices were imaged by scanning electron microscopy (SEM, FEI Apreo LoVac). Photoluminescence (PL) was carried out using a steady-state spectroscope (FLS 1000, Edinburgh Instruments) excited by 468 nm laser. The transient photovoltage decay and the light-intensity-dependent $V_{OC}$ measurements were performed on an electrochemical workstation (ZAHNER, Germany). The current density-voltage (*J-V*) characteristics and steady-state output of the solar cells were measured using a Keithley 2400 source meter. The illumination was provided by a Newport Oriel 92192 solar simulator with an AM1.5G filter, operating at 100 mW/cm$^2$, which was calibrated by a standard silicon solar cell from Newport. both forward and backward scans were performed, and the scan speed was fixed at 0.15 V/s. Devices were exposed to ambient indoor lighting in the laboratory during storage stability tests. The external quantum efficiency (EQE) of the perovskite solar cell device was measured by using a QE-R instrument from Enlitech. For the EQE measurements of tandem solar cells, two light-emitting diodes

with emission wavelength of 550 nm and 850 nm were used as bias illumination to measure NBG and WBG sub-cells, respectively. The space charge limited current (SCLC) of hole-only devices and the EL and $EQE_{EL}$ spectra of the solar devices were recorded simultaneously by a commercialized system (XPQY-EQE-350-1100, Guangzhou Xi Pu Optoelectronics Technology Co., Ltd.), which is equipped with an integrated sphere (GPS-4P-SL, Labsphere) and a photodetector array (S7031-1006, Hamamatsu Photonics).

**Calculation of Decomposition Activation Energy ($E_a$)**

The higher the *E*a value the larger resistance for decomposition, which implies that a higher temperature or longer exposure of heat are required for perovskite films to start degrading. Here, the *E*a values were determined by fitting the measured decomposition rates (*k*) of the perovskite films at various temperatures using the Arrhenius equation[1]:

$$k = A\exp(\frac{-E_a}{RT}) \quad (1)$$

where *k* is the decomposition rate of the perovskite films, *A* ($min^{-1}$) is the pre-exponential factor, $E_a$ (kJ $mol^{-1}$) is the decomposition activation energy, *R* (8.314 J $mol^{-1}$ $K^{-1}$) is the ideal gas constant and *T* (*k*) is the absolute temperature. By plotting ln *k* against 1/T, *E*a can be obtained by fitting the data to using the equation (2):

$$\ln k = \ln A - (\frac{E_a}{R})\frac{1}{T} \quad (2)$$

To determine *k* under thermal stress, we quantified the integral areas of the $PbI_2$ and perovskite characteristic diffraction peaks using the following equation (3) [2-4]:

$$k = \frac{S_{PbI_2}}{(S_{PbI_2} + bS_{PVK})\Delta t} \quad (3)$$

where $S_{PbI_2}$ and $S_{PVK}$ represent the integral areas of the $PbI_2$ and (100)-oriented perovskite diffraction peaks of the three films, respectively. The calibration factor $b$ is defined as the ratio of the $PbI_2$ diffraction areas in a fully decomposed perovskite sample to the (100)-oriented diffraction peak areas in a fresh perovskite sample, while $\Delta t$ represents the thermal aging duration.

Combining the above equations and the measured XRD spectra of the three films for thermal stress at temperatures of 120 °C, 150 °C, 165 °C, 180 °C and 200 °C for varying durations (**Figure S4**), we calculated the ln($k$) values of the films (**Table S2**). On this basis, the ln($k$) versus (1/T) curves are plotted for the all-MA, MA-FA and all-FA samples, as depicted in **Figure S5**. By fitting the ln($k$)-(1/T) curves, the $E_a$ values are therefore determined to be 104.44, 111.68 and 149.13 kJ $mol^{-1}$ for the all-MA, MA-FA and all-FA samples, respectively.

**Density Functional Theory (DFT)**:

DFT calculations were performed using the Vienna ab initio simulation package (VASP) with the standard frozen-core projector augmented-wave (PAW) method. The plane-wave cutoff energy was set to 450 eV, suitable for describing valence electron states in most systems. The generalized gradient approximation (GGA) with the Perdew–Burke–Ernzerh (PBE) functional was employed for exchange-correlation effects, and Grimme's DFT-D3 scheme was incorporated to account for van der Waals interactions. The convergence criterion for the total energy difference was set to $1.0 \times 10^{-5}$ eV (a typical value for self-consistent field calculations), while all atomic positions

were relaxed until the Hellmann–Feynman forces on each atom were below 0.01 eV/Å.

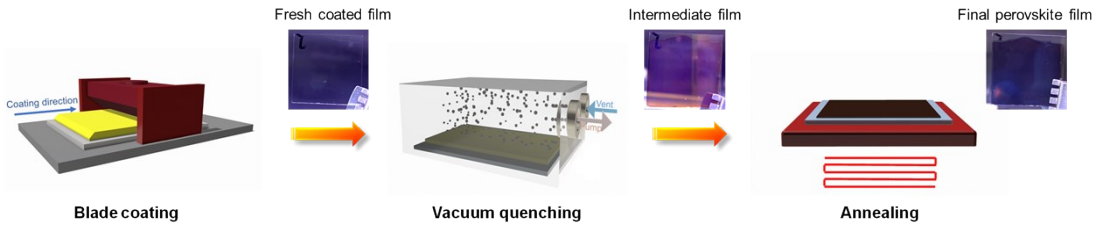


**Figure S1.** The schematic of the preparation of Pb-Sn perovskite thin films.

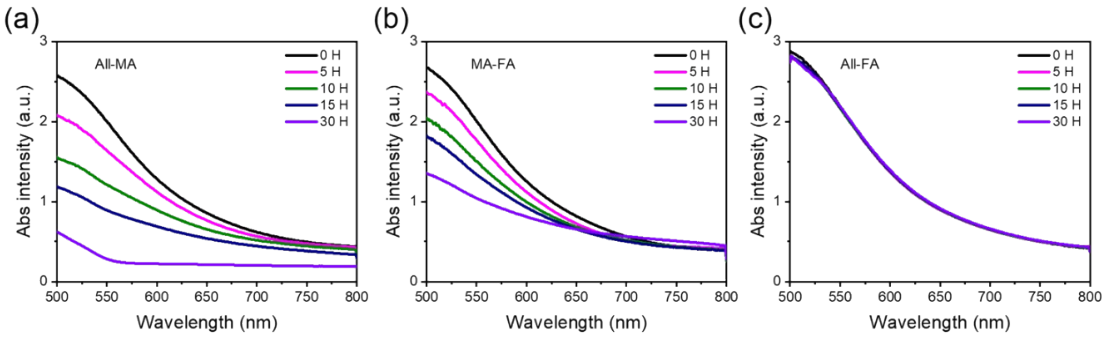


**Figure S2.** UV-visible absorption spectra of (a) all-MA, (b) MA-FA and (c) all-FA samples under thermal stress of 120 °C for 0, 5, 10, 15 and 30 h.

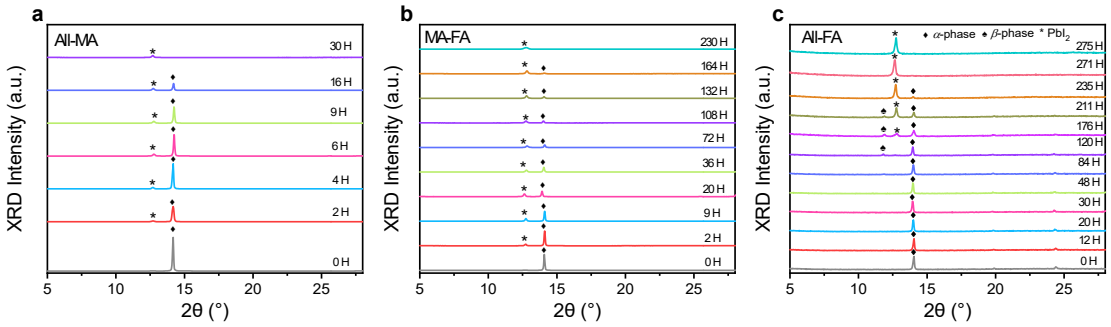


**Figure S3.** XRD diffraction patterns of (a) all-MA, (b) MA-FA, (c) all-FA samples after thermal stressing at 120 °C for various time. Note: in the XRD patterns, the '⋖' symbol marks the $PbI_2$ diffraction peak, the '♦' symbol marks the (100) diffraction peak of $\alpha$-phase perovskite, and the '♠' symbol represents the characteristic peak (at ~11.9º) of $\beta$-phase perovskite.

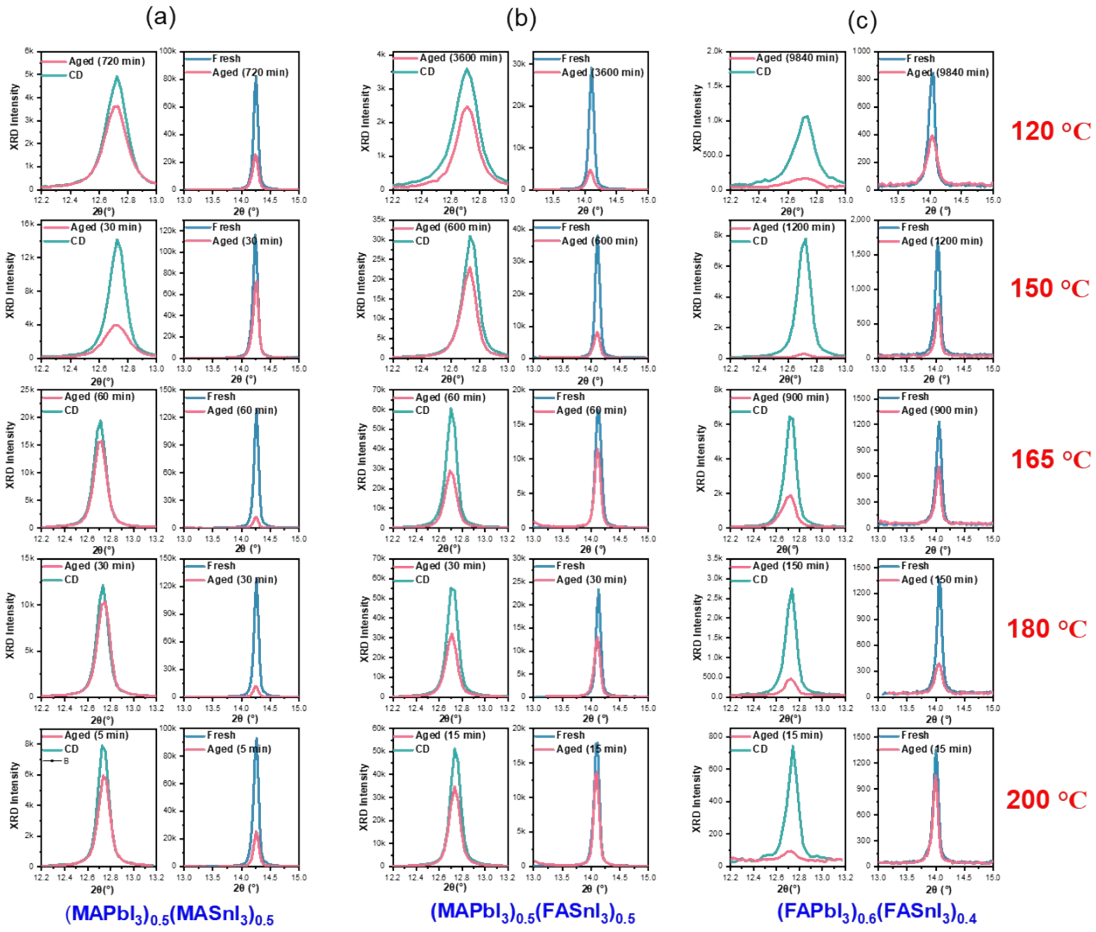


**Figure S4.** XRD pattern of (a) all-MA, (b) MA-FA, (c) all-FA samples annealed at 120 ℃, 150 ℃, 165 ℃, 180 ℃ for various time.

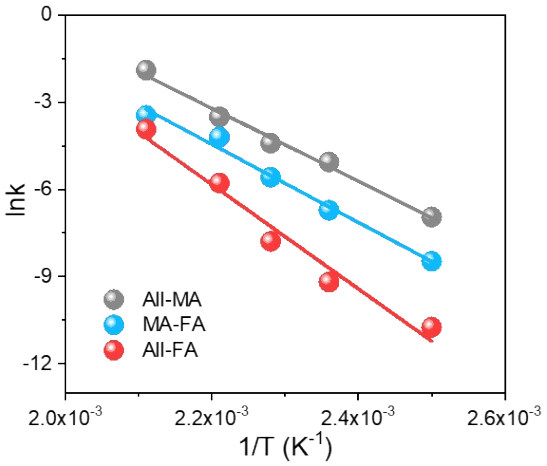


**Figure S5.** The plot of ln(k) versus (1/T) of the three films.

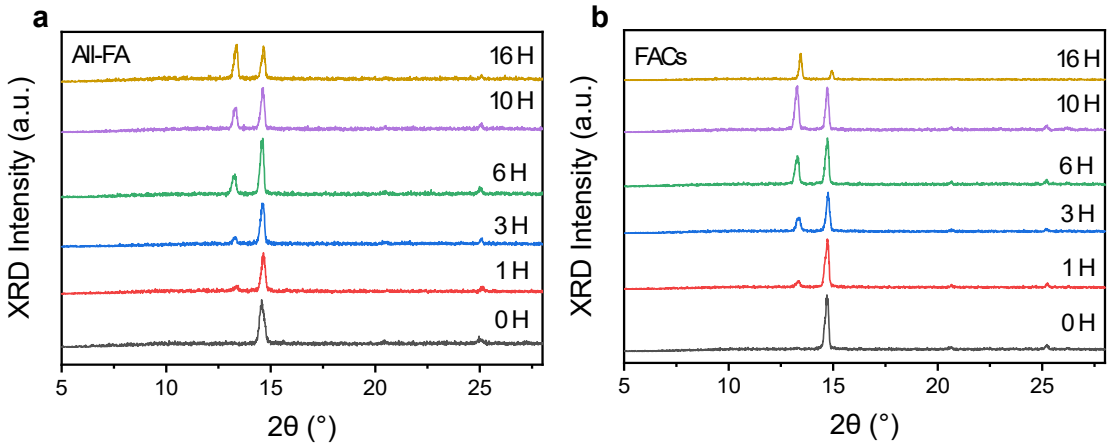


**Figure S6.** XRD pattern of (a) all-FA- and (b) FACs-based perovskite films under continuous thermal stress at 165 °C.

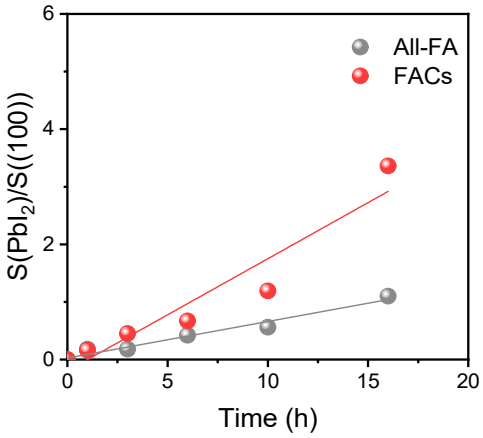


**Figure S7.** Diffraction peak area ratio of $PbI_2$ to perovskite (100) peak, extracted from the XRD patterns shown in **Figure S5**.

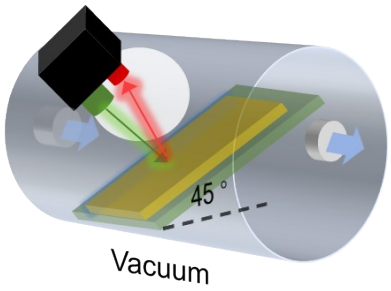


**Figure S8.** Schematic of the in-situ PL setup, which consists of a vacuum chamber, a laser, a fiber optic prob, and a pressure control system driven by an Edwards RV12 vacuum pump.

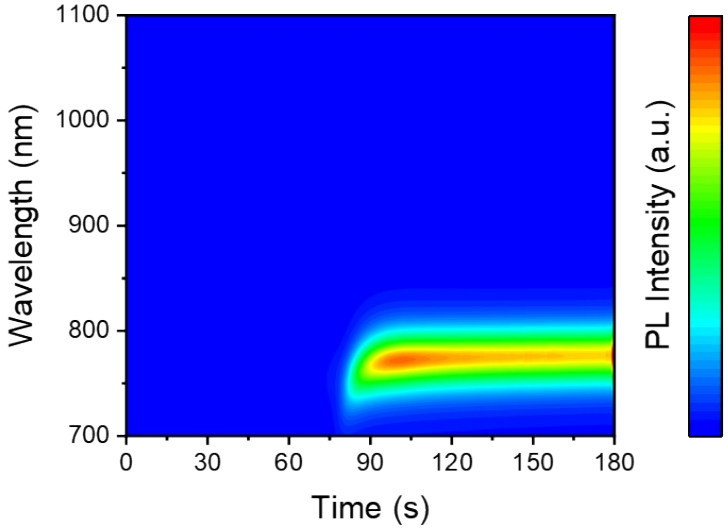


**Figure S9.** 2D contour maps of the in-situ PL spectra for $FA_{0.85}MA_{0.10}Cs_{0.05}PbI_3$ wet films during the vacuum-quenching process.

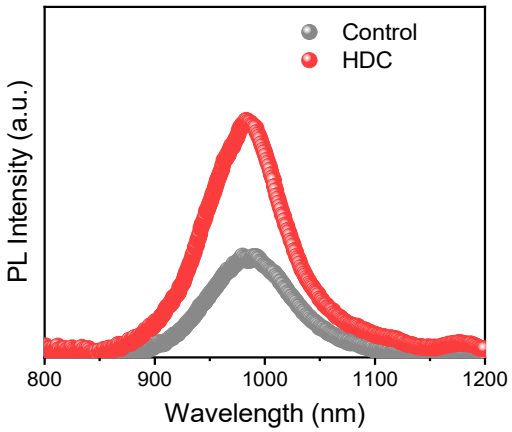


**Figure S10.** Steady-state PL spectra of the control and HDC-processed $FAPb_{0.5}Sn_{0.5}I_3$ films deposited on glass.

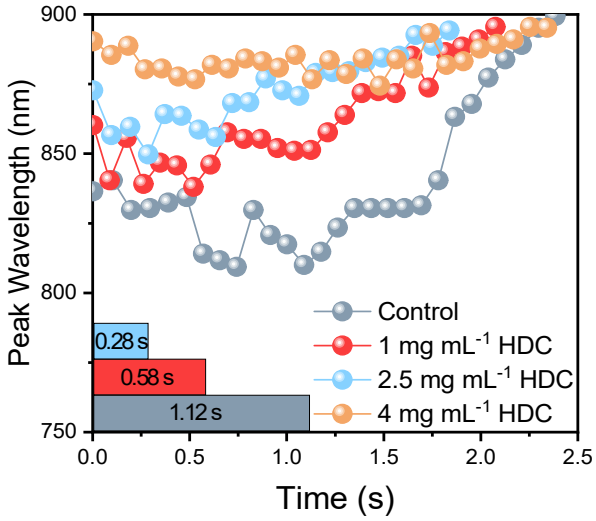


**Figure S11.** The left-hand PL peak evolution of four films during the thermal annealing.

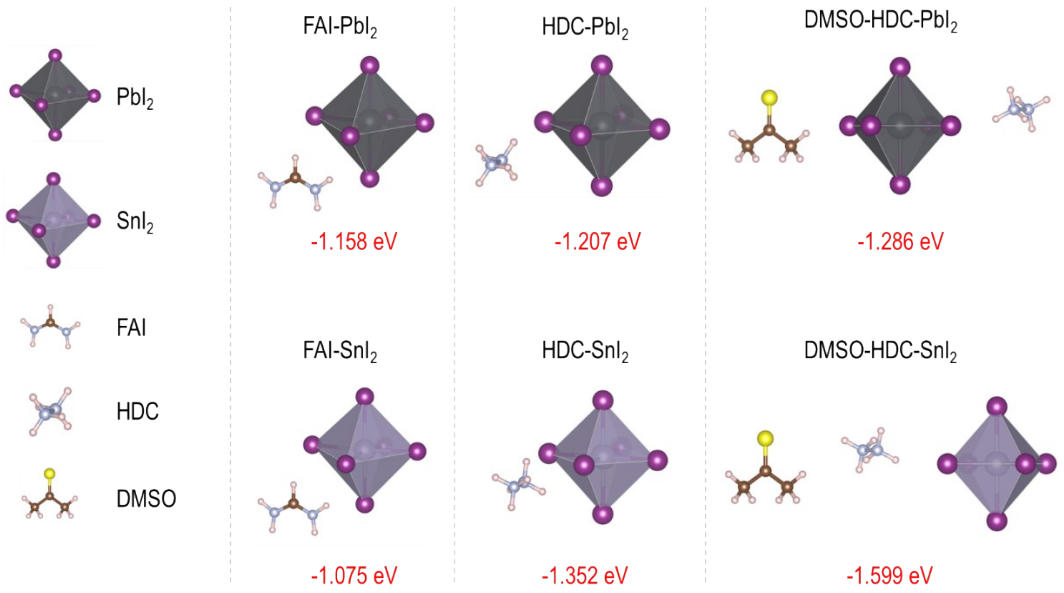


**Figure S12.** The DFT-simulated binding energies between $BX_2$ ($SnI_2$ and $PbI_2$) and FAI, as well as between $BX_2$ and HDC-induced intermediate states.

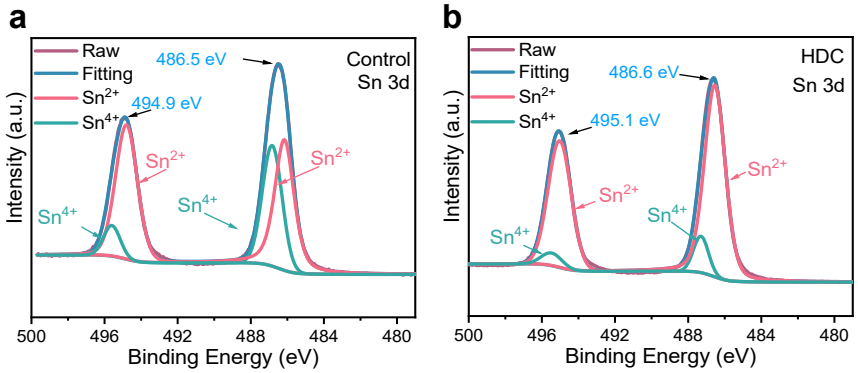


**Figure S13.** The Sn 3d XPS spectra of (a) the control film and (b) the HDC-processed film. (f) XRD patterns of the control, and 1, 2.5, 4 mg $mL^{-1}$ HDC-processed perovskite films.

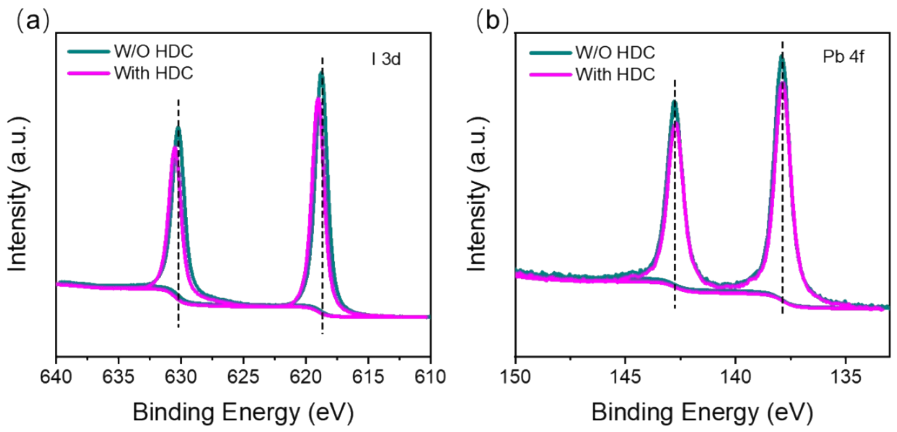


**Figure S14.** (a) I 3d XPS spectra and (b) Pb 4f XPS spectra of the all-FA Pb-Sn perovskite films without (w/o) and with HDC.

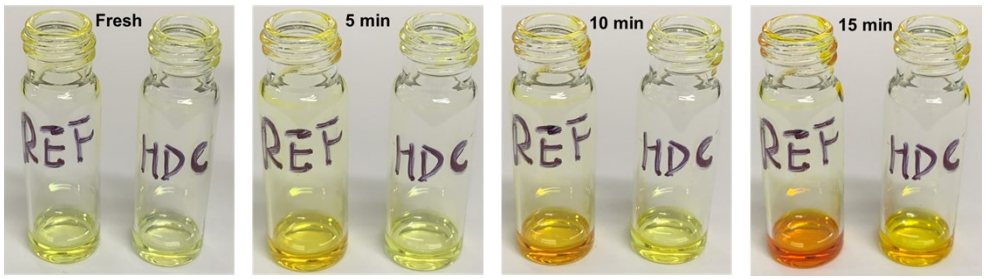


**Figure S15.** The photographs of Pb-Sn perovskite precursor solutions without (noted as ref) and with (noted as HDC) HDC exposed to ambient air for varying durations.

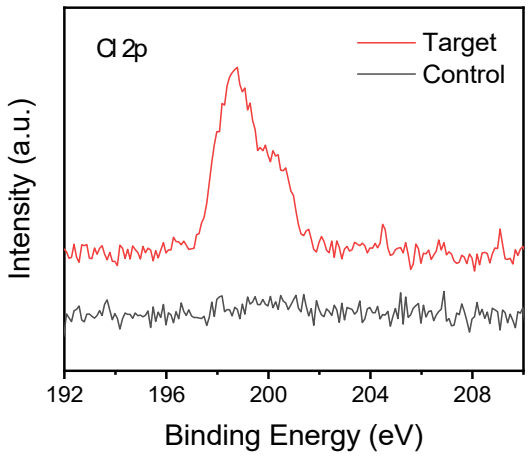


**Figure S16.** The Cl 2p XPS spectra of control and HDC-processed films.

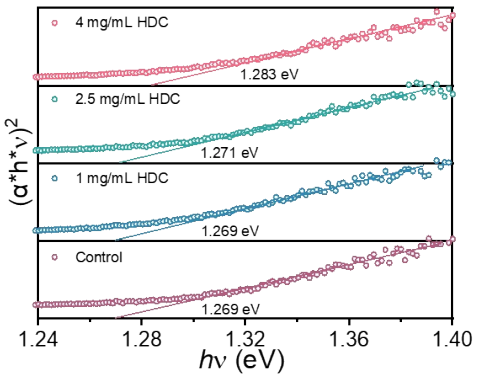


**Figure S17.** The bandgap of all-FA Pb-Sn perovskite with different HDC concentration.

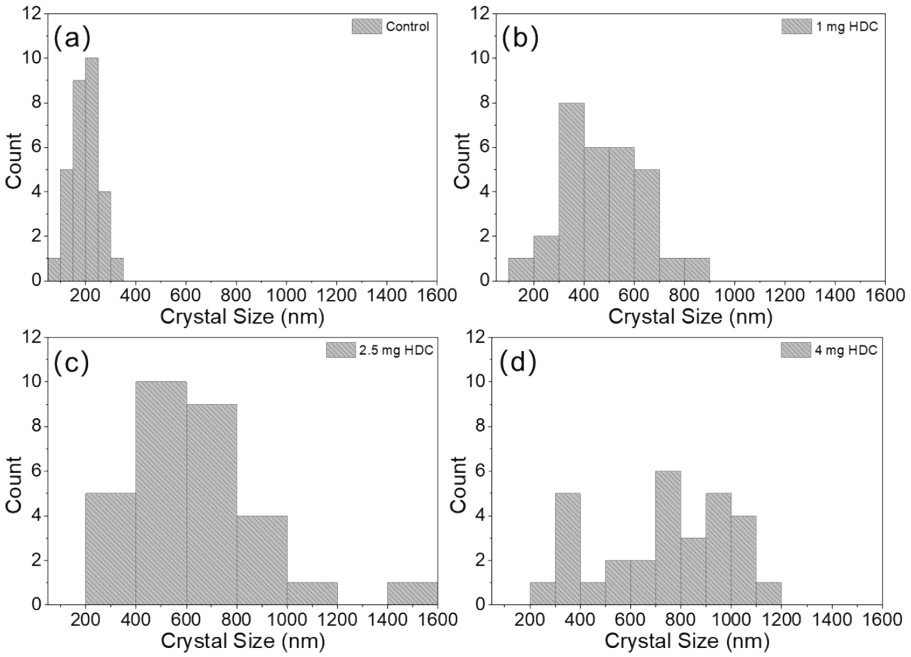


**Figure S18.** The grain size distribution of (a) the control, (b) 1mg/mL HDC-processed, (c) 2.5 mg/mL HDC-processed and (d) 4 mg/mL HDC-processed perovskite films.

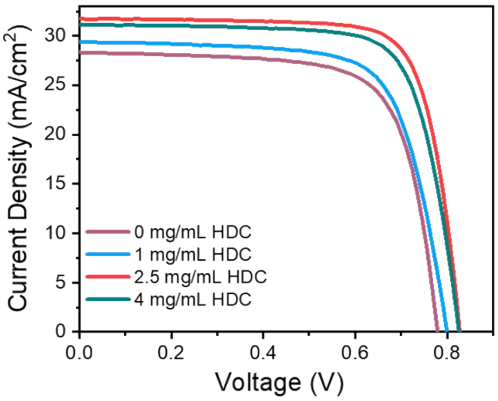


**Figure S19.** The J-V curves of the all-FA Pb-Sn PSCs with different HDC concentration.

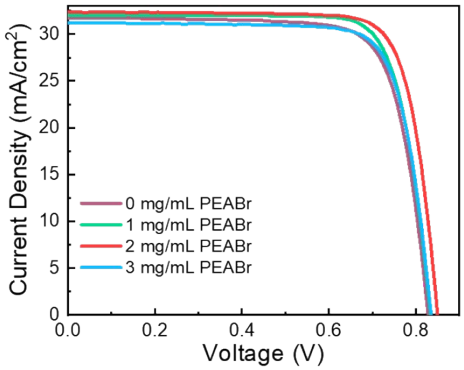


**Figure S20.** The J-V curves of the 2.5 mg/mL HDC-processed all-FA based Pb-Sn mixed PSCs with different PEABr passivation concentration.

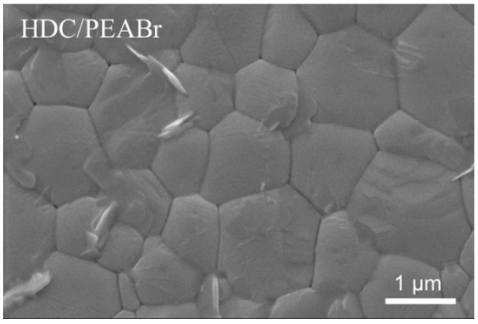


**Figure S21.** Top-view SEM image of the HDC/PEABr-processed all-FA Pb-Sn perovskite film.

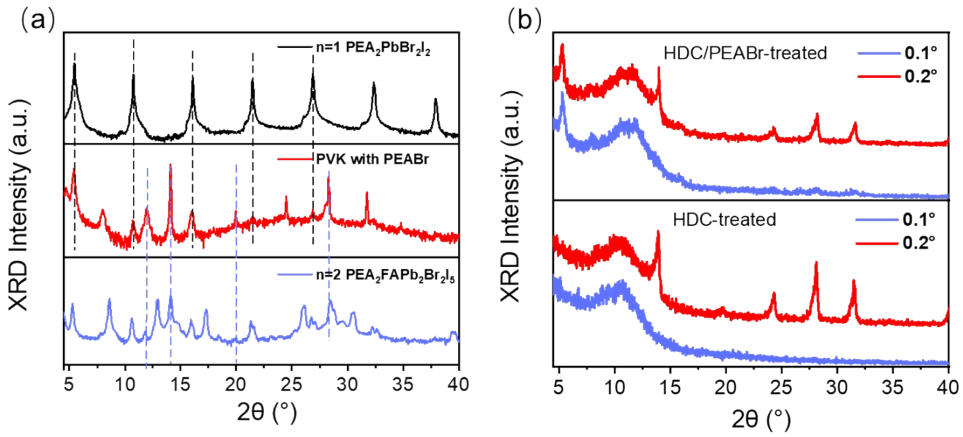


**Figure S22.** (a) XRD patterns of the n=1 of 2D $PEA_2PbBr_2I_2$ perovskite (top), 3D PEABr-processed perovskite (middle) and the n=2 of 2D $PEA_2FAPb_2Br_2I_5$ perovskite (bottom) films. (b) GI-XRD patterns of the HDC/PEABr-processed and HDC-processed perovskite films at incident angle of 0.1° and 0.2°.

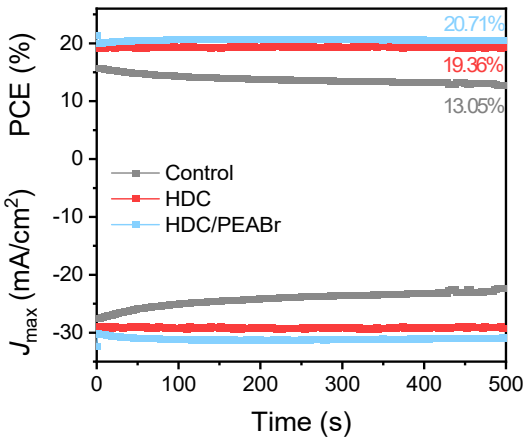


**Figure S23.** The steady-state output measurement of the control, HDC- and HDC/PEABr-processed device.

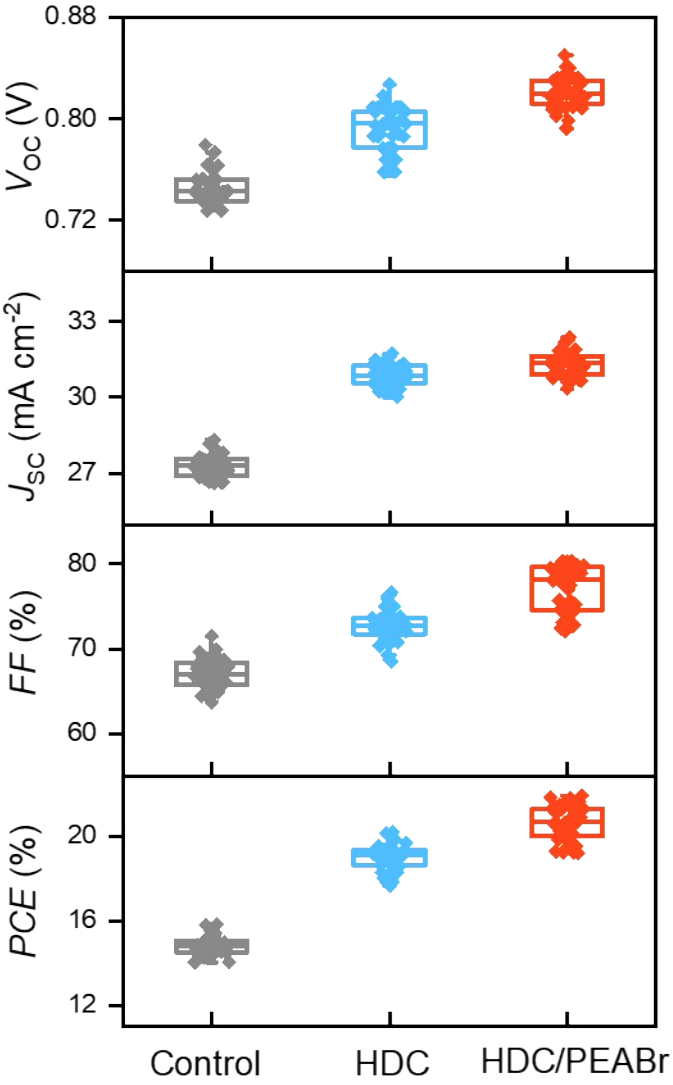


**Figure S24.** $V_{OC}$, $J_{SC}$, *FF*, *PCE* parameters of the three devices (40 cells).

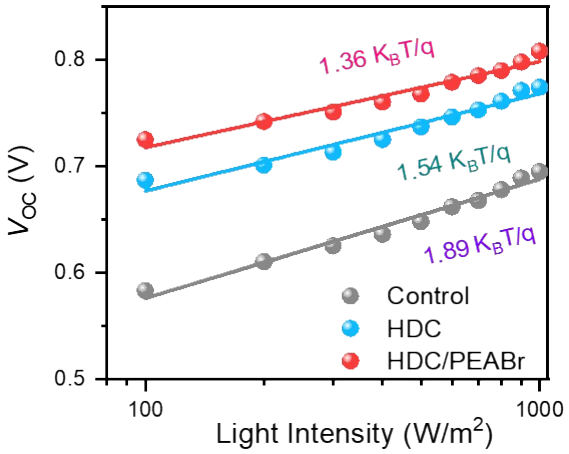


**Figure S25.** $V_{OC}$ as a function of light intensity in a semi-log plot of the control, HDC- and HDC/PEABr-processed PSCs.

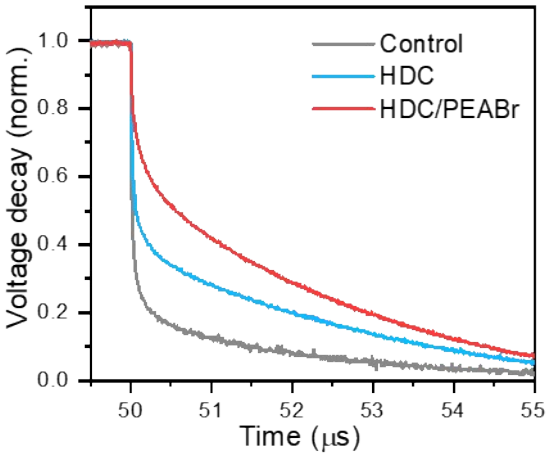


**Figure S26.** Transient photovoltage (TPV) of the control, HDC- and HDC/PEABr-processed PSCs.

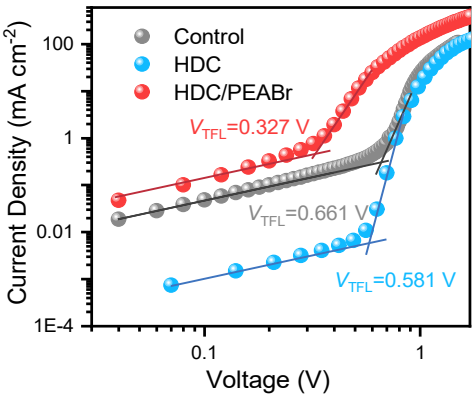


**Figure S27.** SCLC curves of the hole-only device (ITO/PEDOT:PSS/perovskite/ PTAA/Ag) based on the three perovskites.

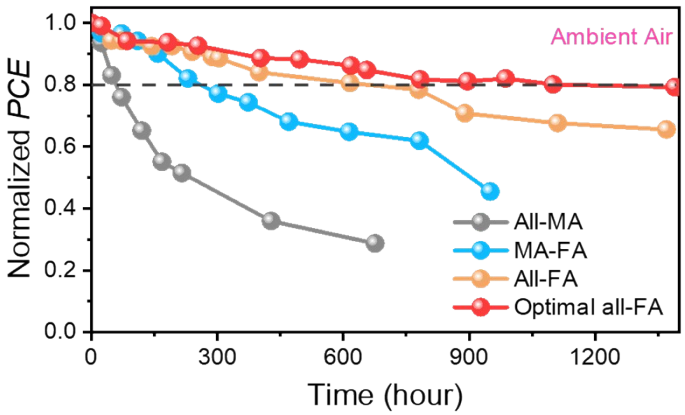


**Figure S28.** Shelf stability of the all-MA, MA-FA, all-FA and HDC/PEABr-processed all-FA devices under ambient air.

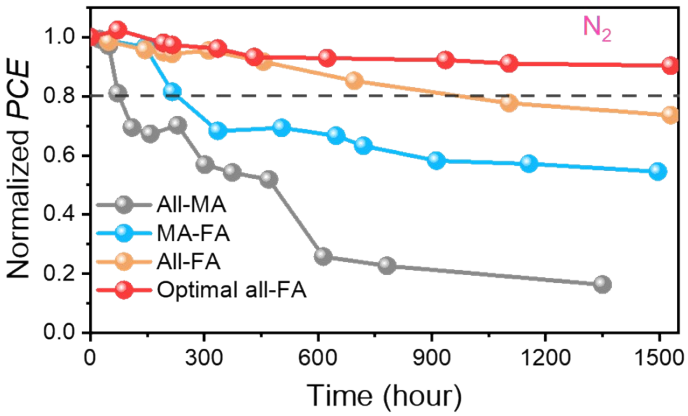


**Figure S29.** Shelf stability of the all-MA, MA-FA, all-FA and HDC/PEABr-processed all-FA devices under $N_2$-filled glove box.

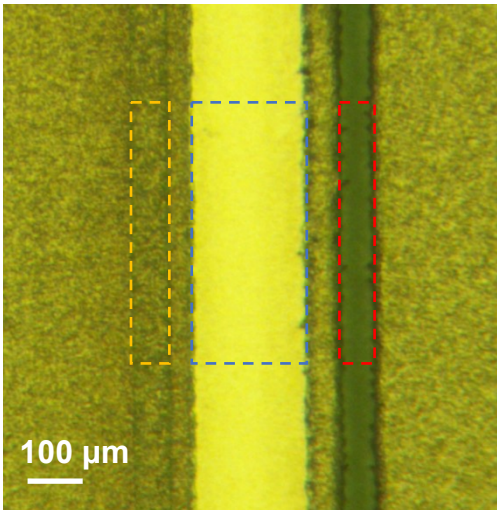


**Figure S30**. Optical microscope image of the interconnection region of the module. The orange dashed box highlights the P1 scribe, the blue dashed box indicates the P2 scribe, and the red dashed box marks the P3 scribe.

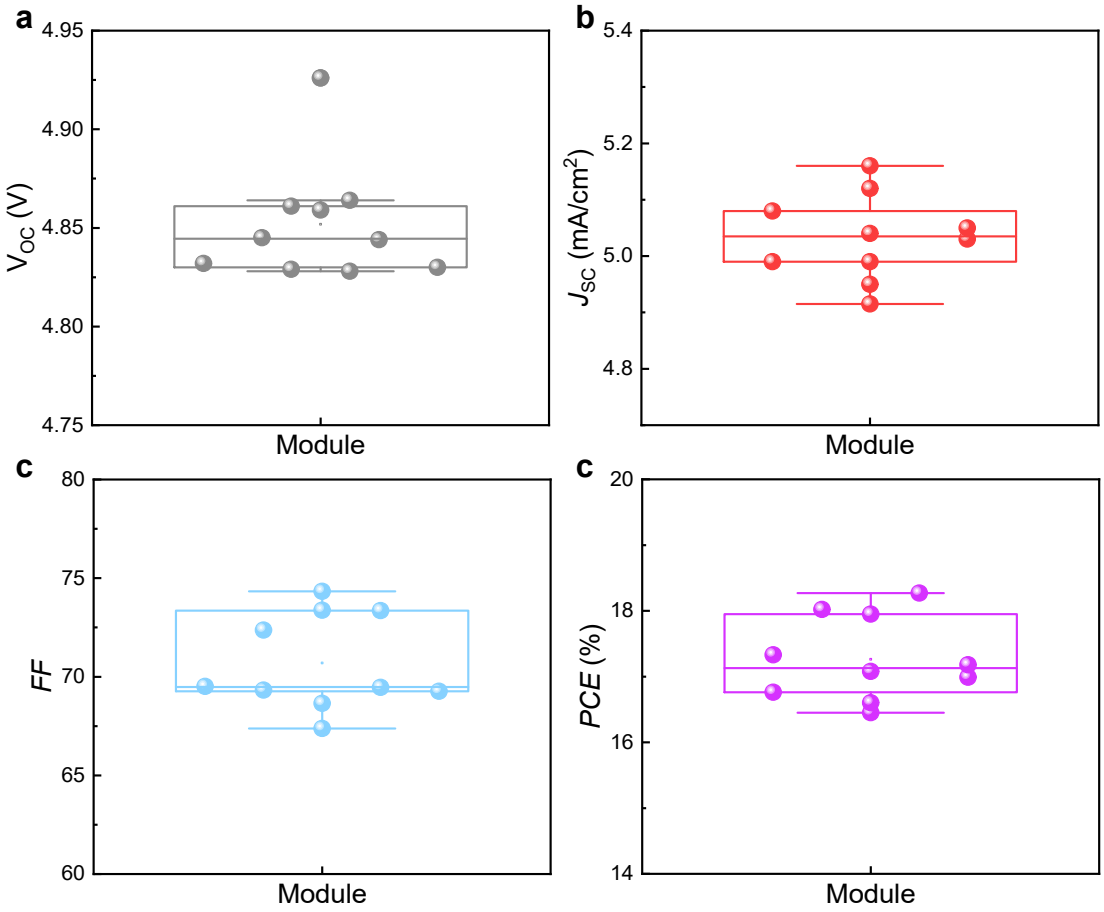


**Figure S31**. (a) $V_{OC}$, (b) $J_{SC}$, (c) *FF*, (d) *PCE* parameters of 5 cm × 5 cm modules (10 cells).

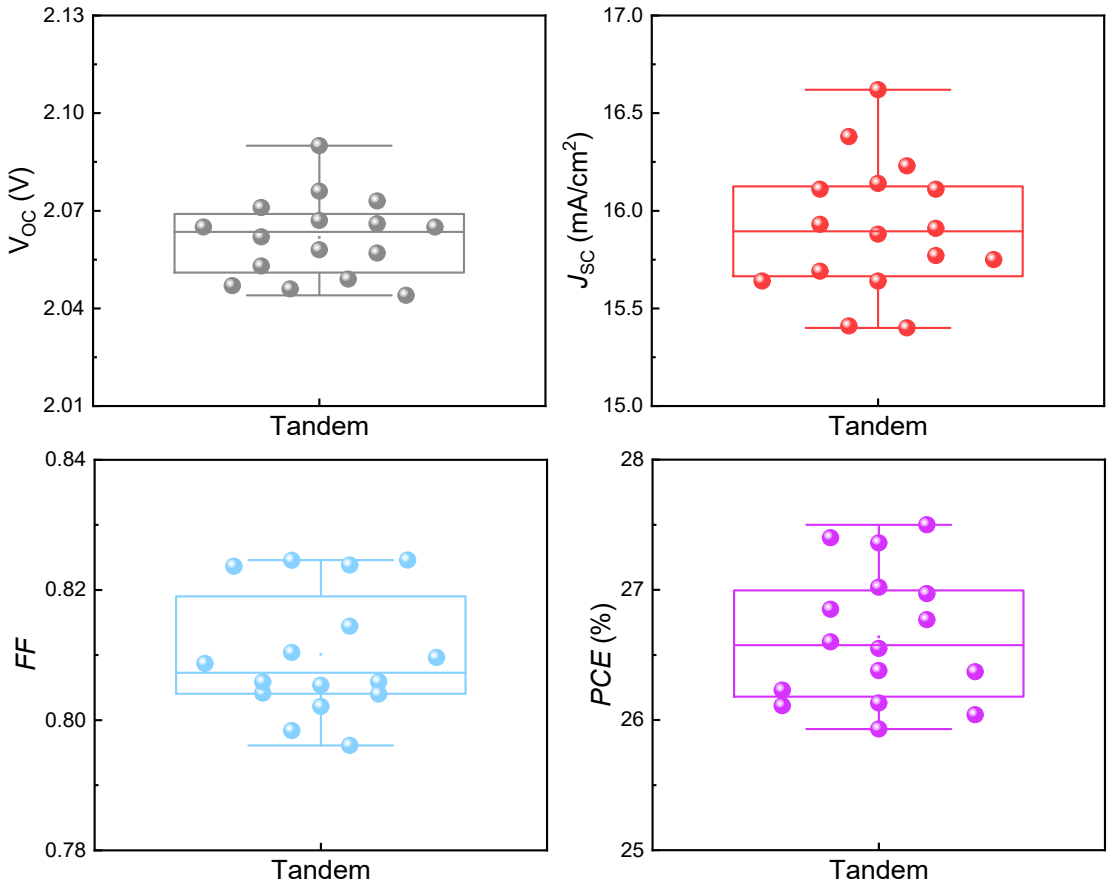


**Figure S32**. (a) $V_{OC}$, (b) $J_{SC}$, (c) *FF*, (d) *PCE* parameters of Tandem devices (16 cells).

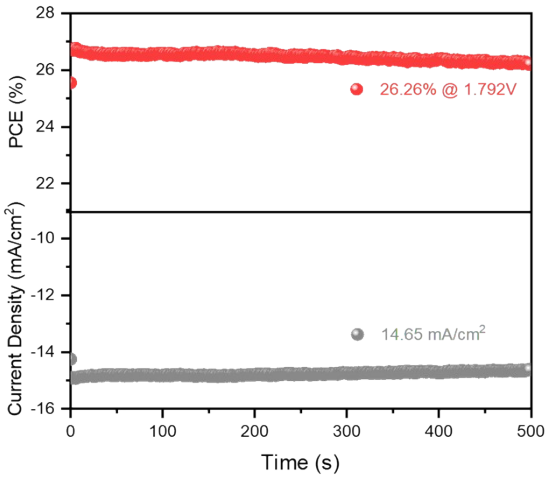


**Figure S33.** The steady-state output measurement of the all-perovskite tandem solar cells.

**Table S1.** Average absorption intensity between 500 and 800 nm of all-MA, MA-FA and all-FA samples after thermal stressing at 120 °C for 0, 5, 10, 15, 30 hours.

| Time of thermal stressing at 120 °C | Average absorption intensity of all-MA sample (500 nm-800 nm) | Average absorption intensity of MA-FA sample (500 nm-800 nm) | Average absorption intensity of all-FA sample (500 nm-800 nm) |
|---|---|---|---|
| 0 h | 1.12 | 1.10 | 1.21 |
| 5 h | 0.97 | 0.99 | 1.20 |
| 10 h | 0.78 | 0.89 | 1.20 |
| 15 h | 0.62 | 0.82 | 1.21 |
| 30 h | 0.25 | 0.75 | 1.21 |

**Table S2.** The calculation of ln(k) value of three perovskite films annealed at 120 ℃, 150 ℃, 165 ℃, 180 ℃ and 200 ℃.

| | | $S_{PVK}$ | $S_{PbI2}$ | Δt (min) | D-$S_{PbI2}$ | F-$S_{PVK}$ | b | ( $S_{PVK}$ +$S_{PbI2}$*b)*Δt | k | lnk |
|---|---|---|---|---|---|---|---|---|---|---|
| 120 | MA | 3455.8 | 852.4839 | 720 | 1017 | 9053.3882 | 0.1123336 | 893294.1114 | 0.000954315 | -6.954516834 |
| | MAFA | 681.77 | 533.7722 | 3600 | 826.44815 | 3174.15825 | 0.2603677 | 2560616.245 | 0.000208455 | - 8.475789352 |
| | FA | 125.45 | 66.51 | 9840 | 299.29 | 150.82 | 1.9844185 | 3104080.175 | 2.14266E-05 | -10.75087568 |
| 150 | MA | 9990 | 1036.7 | 60 | 2443.27 | 14440.523 | 0.1691954 | 163617.4155 | 0.006336123 | -5.061488279 |
| | MAFA | 1293.8 | 3580.51 | 600 | 4602.47 | 4397.99 | 1.046494 | 2960697.173 | 0.001209347 | -6.717674803 |
| | FA | 129.68 | 73.05 | 1200 | 1101.83 | 272.18 | 4.0481667 | 717619.5021 | 0.000101795 | -9.192550628 |
| 165 | MA | 4004.6 | 2684.135 | 60 | 3123.01 | 12326.78 | 0.2533516 | 221922.116 | 0.012094941 | -4.414967976 |
| | MAFA | 1778 | 4358.93 | 120 | 7799.17 | 2603.79 | 2.9953145 | 112151.906 | 0.00375074 | -5.585802043 |
| | FA | 111.45 | 323.389 | 900 | 913.0535 | 187.3517 | 4.8734733 | 779886.2476 | 0.000414662 | -7.788047419 |
| 180 | MA | 1415.2 | 1547.814 | 30 | 1686.366 | 14767.6123 | 0.1141935 | 51282.68864 | 0.03018199 | -3.500509887 |
| | MAFA | 2000 | 4632.85 | 30 | 7942.8 | 2760.575 | 2.8772267 | 311618.2367 | 0.01486707 | -4.208606609 |
| | FA | 94.56 | 146.257 | 150 | 437.347 | 242.353 | 1.8045867 | 47534.80772 | 0.00307684 | -5.783852168 |
| 200 | MA | 3314.4 | 998.357 | 5 | 1226.6578 | 12044.1832 | 0.1018465 | 6679.605933 | 0.149463458 | -1.900703345 |
| | MAFA | 1944.9 | 4851.48 | 15 | 6851.291 | 2490.0882 | 2.751425 | 153042.549 | 0.031700204 | -3.451432167 |
| | FA | 183.05 | 49.07 | 15 | 150.37335 | 235.2944 | 0.639086 | 2490.820304 | 0.019700337 | -3.927119524 |

**Table S3.** The detailed performance parameters of the all-FA Pb-Sn PSCs with different HDC concentration.

| HDC concentration | $V_{OC}$ (V) | $J_{SC}$ (mA/cm$^2$) | FF | PCE (%) |
|---|---|---|---|---|
| 0 mg/mL | 0.779 | 28.33 | 0.72 | 15.81 |
| 1 mg/mL | 0.801 | 29.38 | 0.71 | 16.70 |
| 2.5 mg/mL | 0.827 | 31.72 | 0.77 | 20.12 |
| 4 mg/mL | 0.825 | 31.12 | 0.75 | 19.14 |

**Table S4**. The detailed performance parameters of the 2.5mg/mL HDC-processed all-FA Pb-Sn PSCs with different PEABr concentration.

| PEABr passivation concentration | $V_{OC}$ (V) | $J_{SC}$ (mA/cm$^2$) | FF | PCE (%) |
|---|---|---|---|---|
| 0 mg | 0.827 | 31.72 | 0.77 | 20.12 |
| 1 mg | 0.833 | 32.01 | 0.79 | 21.05 |
| 2 mg | 0.850 | 32.36 | 0.80 | 21.81 |
| 3 mg | 0.835 | 31.20 | 0.78 | 20.36 |

**Table S5.** The previous reported All-FA Pb-Sn PSCs

| Components | Preparation method of perovskite | $V_{OC}$ (V) | $J_{SC}$ (mA/cm$^2$) | *FF* (%) | *PCE* (%) | Year [ref] |
|---|---|---|---|---|---|---|
| $FAPb_{0.5}Sn_{0.5}I_3$ | Spin coated | 0.70 | 21.9 | 66.00 | 10.2 | 2016 [5] |
| $FAPb_{0.5}Sn_{0.5}I_3$ | Spin coated | 0.782 | 28.51 | 73.00 | 16.27 | 2018 [6] |
| $FAPb_{0.5}Sn_{0.5}I_3$ | Spin coated | 0.720 | 24.50 | 79.30 | 13.98 | 2019 [7] |
| $FAPb_{0.5}Sn_{0.5}I_3$ | Spin coated | 0.690 | 26.56 | 73.00 | 13.33 | 2020 [8] |
| $FAPb_{0.5}Sn_{0.5}I_3$ | Spin coated | 0.841 | 31.70 | 78.90 | 21.04 | 2022 [9] |
| $FAPb_{0.5}Sn_{0.5}I_3$ | Spin coated | 0.690 | 26.93 | 74.00 | 13.74 | 2022 [10] |
| $FAPb_{0.5}Sn_{0.5}I_3$ | Spin coated | 0.843 | 32.00 | 79.30 | 21.30 | 2023 [11] |
| $FAPb_{0.5}Sn_{0.5}I_3$ | Spin coated | 0.846 | 31.09 | 78.00 | 20.53 | 2023 [12] |
| $FAPb_{0.5}Sn_{0.5}I_3$ | Spin coated | 0.846 | 31.39 | 79.50 | 21.12 | 2024 [13] |

**Table S5** (continued)

| Components | Preparation method of perovskite | $V_{OC}$ (V) | $J_{SC}$ (mA/cm$^2$) | *FF* (%) | *PCE* (%) | Year [ref] |
|---|---|---|---|---|---|---|
| $FAPb_{0.5}Sn_{0.5}I_3$ | Spin coated | 0.875 | 31.87 | 76.10 | 21.22 | 2024 [14] |
| $FAPb_{0.5}Sn_{0.5}I_3$ | Spin coated | 0.895 | 32.68 | 83.2 | 24.33 | 2025 [1] |
| $FAPb_{0.5}Sn_{0.5}I_3$ | Blade-coated | 0.740 | 25.66 | 54.06 | 10.26 | 2024 [15] |
| $FAPb_{0.5}Sn_{0.5}I_3$ | Blade-coated | 0.856 | 30.21 | 78.13 | 20.16 | 2025 [16] |
| $FAPb_{0.5}Sn_{0.5}I_3$ | Blade-coated | 0.850 | 32.36 | 80.00 | 21.81 | This work |

**Table S6.** The previous reported MA-free all-perovskite tandem solar cells.

| Components | Preparation method of perovskite | $V_{OC}$ (V) | $J_{SC}$ (mA/cm$^2$) | *FF* (%) | *PCE* (%) | Year [ref] |
|---|---|---|---|---|---|---|
| $FA_{0.75}Cs_{0.25}Pb_{0.5}Sn_{0.5}I_3$/ $FA_{0.83}Cs_{0.17}Pb(I_{0.5}Br_{0.5})_3$ | Spin coated | 1.66 | 14.5 | 70 | 16.9 | 2016 [5] |
| $FA_{0.75}Cs_{0.25}Pb_{0.5}Sn_{0.5}I_3$/ $FA_{0.6}Cs_{0.4}Pb(I_{0.7}Br_{0.3})_3$ | Spin coated | 1.81 | 14.8 | 70 | 19.1 | 2018 [17] |
| $FA_{0.75}Cs_{0.25}Pb_{0.5}Sn_{0.5}I_3$/ $FA_{0.6}Cs_{0.3}DMA_{0.1}Pb(I_{0.8}Br_{0.2})_3$ | Spin coated | 1.88 | 16 | 77 | 23.1 | 2019 [18] |
| $FA_{0.8}Cs_{0.2}Pb_{0.5}Sn_{0.5}I_3$/ $FA_{0.8}Cs_{0.2}Pb(I_{0.6}Br_{0.4})_3$ | Spin coated | 1.9 | 15.4 | 80.4 | 23.5 | 2021 [19] |
| $FA_{0.8}Cs_{0.2}Pb_{0.5}Sn_{0.5}I_3$/ $FA_{0.6}Cs_{0.4}PbI_{2.04}Br_{0.96}$ | Spin coated | 2.03 | 15.4 | 78 | 24.4 | 2022 [20] |
| $FA_{0.8}Cs_{0.2}Pb_{0.5}Sn_{0.5}I_3$/ $FA_{0.6}Cs_{0.4}PbI_2Br$ | Spin coated | 2.03 | 15.8 | 79.4 | 25.6 | 2022 [21] |
| $FA_{0.8}Cs_{0.2}Pb_{0.5}Sn_{0.5}I_3$/ $FA_{0.6}Cs_{0.4}PbI_{2.16}Br_{0.84}$ | Spin coated | 2.05 | 16.2 | 79 | 26.3 | 2022 [22] |
| $FAPb_{0.5}Sn_{0.5}I_3$/ $FA_{0.8}Cs_{0.2}Pb(I_{0.6}Br_{0.4})_3$ | Spin coated | 2.135 | 16.2 | 81.5 | 28.1 | 2023 [11] |
| $FA_{0.8}Cs_{0.2}Pb_{0.5}Sn_{0.5}I_3$/ $FA_{0.8}Cs_{0.2}Pb(I_{0.6}Br_{0.4})_3$ | Spin coated | 2.04 | 15.1 | 82.1 | 25.3 | 2023 [23] |

**Table S6** (continued)

| Components (NBG/WBG) | Preparation method of perovskite | $V_{OC}$ (V) | $J_{SC}$ (mA/cm$^2$) | *FF* (%) | *PCE* (%) | Year [ref] |
|---|---|---|---|---|---|---|
| $FA_{0.8}Cs_{0.2}Pb_{0.5}Sn_{0.5}I_3$/ $FA_{0.8}Cs_{0.2}Pb(I_{0.6}Br_{0.4})_3$ | Spin coated | 2.11 | 15.8 | 81 | 27.0 | 2024 [24] |
| $FA_{0.8}Cs_{0.2}Pb_{0.5}Sn_{0.5}I_3$/ $FA_{0.8}Cs_{0.2}Pb(I_{0.6}Br_{0.4})_3$ | Spin coated | 2.13 | 15.58 | 82.6 | 27.4 | 2024 [25] |
| $FA_{0.75}Cs_{0.25}Pb_{0.5}Sn_{0.5}I_3$/ $FA_{0.8}Cs_{0.2}Pb(I_{0.6}Br_{0.4})_3$ | Spin coated | 2.22 | 16.45 | 80.33 | 29.33 | 2025 [26] |
| $FA_{0.75}Cs_{0.25}Pb_{0.5}Sn_{0.5}I_3$/ $FA_{0.8}Cs_{0.2}Pb(I_{0.63}Br_{0.37})_3$ | Spin coated | 2.156 | 15.63 | 81.93 | 27.61 | 2025 [27] |
| $FAPb_{0.5}Sn_{0.5}I_3$/ $FA_{0.8}Cs_{0.2}Pb(I_{0.6}Br_{0.4})_3$ | Blade-coated | 2.08 | 15.41 | 81.86 | 26.23 | 2025 [16] |
| $FAPb_{0.5}Sn_{0.5}I_3$/ $FA_{0.8}Cs_{0.2}Pb(I_{0.6}Br_{0.4})_3$ | Blade-coated | 2.065 | 16.11 | 82.00 | 27.40 | This work |

## Reference


1. F. Yao, Q. Wu, Y. Lei, W. Guo and Y. Xu, *Polymer Degradation and Stability*, 2008, **93**, 90-98.
2. W. Tan, A. R. Bowring, A. C. Meng, M. D. McGehee and P. C. McIntyre, *ACS Applied Materials & Interfaces*, 2018, **10**, 5485-5491.
3. W. Yang, D. Zhong, M. Shi, S. Qu and H. Chen, *iScience*, 2019, **22**, 534-543.
4. H. Zheng, G. Liu, W. Wu, H. Xu and X. Pan, *Journal of Energy Chemistry*, 2021, **57**, 593-600.
5. G. E. Eperon, T. Leijtens, K. A. Bush, R. Prasanna, T. Green, J. T.-W. Wang, D. P. McMeekin, G. Volonakis, R. L. Milot, R. May, A. Palmstrom, D. J. Slotcavage, R. A. Belisle, J. B. Patel, E. S. Parrott, R. J. Sutton, W. Ma, F. Moghadam, B. Conings, A. Babayigit, H.-G. Boyen, S. Bent, F. Giustino, L. M. Herz, M. B. Johnston, M. D. McGehee and H. J. Snaith, *Science*, 2016, **354**, 861-865.
6. S. Shao, Y. Cui, H. Duim, X. Qiu, J. Dong, G. H. ten Brink, G. Portale, R. C. Chiechi, S. Zhang, J. Hou and M. A. Loi, *Advanced Materials*, 2018, **30**, 1803703.
7. A. M. Igual-Muñoz, J. Ávila, P. P. Boix and H. J. Bolink, *Solar RRL*, 2020, **4**, 1900283.
8. C. Park, J. Choi, J. Min and K. Cho, *ACS Energy Letters*, 2020, **5**, 3285-3294.
9. P. Wu, J. Wen, Y. Wang, Z. Liu, R. Lin, H. Li, H. Luo and H. Tan, *Advanced Energy Materials*, 2022, **12**, 2202948.
10. L. Wang, Z. Wang, H. Li, B. Chang, L. Pan, Z. Xie and L. Yin, *ACS Applied Materials & Interfaces*, 2022, **14**, 18302-18312.
11. J. Wen, Y. Zhao, P. Wu, Y. Liu, X. Zheng, R. Lin, S. Wan, K. Li, H. Luo, Y. Tian, L. Li and H. Tan, *Nature Communications*, 2023, **14**, 7118.
12. Y. Zhou, Z. Wang, J. Jin, X. Zhang, J. Zou, F. Yao, Z. Zhu, X. Cui, D. Zhang, Y. Yu, C. Chen, D. Zhao, Q. Cao, Q. Lin and Q. Tai, *Angewandte Chemie International Edition*, 2023, **62**, e202300759.
13. Y. Zhou, T. Guo, J. Jin, Z. Zhu, Y. Li, S. Wang, S. Zhou, Q. Lin, J. Li, W. Ke, G. Fang, X. Zhang and Q. Tai, *Energy & Environmental Science*, 2024, **17**, 2845-2855.
14. J. Wang, X. Zheng, C. Zhang, C. Chen, Q. Yao, T. Niu, L. Chao, Q. Guo, H. Zhang, Y. Xia, M. Li, H. Lu, H. Do, Z. Chen, G. Xing, Z. Hu and Y. Chen, *Nano Energy*, 2024, **128**, 109851.
15. A. Tara, V. Schröder, A. Paul, N. Maticiuc, M. F. Vasquez-Montoya, J. Dagar, S. Sharma, R. Gupta, E. J. W. List-Kratochvil, E. L. Unger and F. Mathies, *ACS Applied Materials & Interfaces*, 2024, **16**, 63520-63527.
16. Y. Liu, H. Li, J. Wei, W. Feng, B. Tu, W. Peng, Z. Chen, L. Zeng, Y. Mai and F. Guo, *Nano Energy*, 2025, **141**, 111093.
17. T. Leijtens, R. Prasanna, K. A. Bush, G. E. Eperon, J. A. Raiford, A. Gold-Parker, E. J. Wolf, S. A. Swifter, C. C. Boyd, H.-P. Wang, M. F. Toney, S. F. Bent and M. D. McGehee, *Sustainable Energy & Fuels*, 2018, **2**, 2450-2459.
18. A. F. Palmstrom, G. E. Eperon, T. Leijtens, R. Prasanna, S. N. Habisreutinger, W. Nemeth, E. A. Gaulding, S. P. Dunfield, M. Reese, S. Nanayakkara, T. Moot, J. Werner, J. Liu, B. To, S. T. Christensen, M. D. McGehee, M. F. A. M. van Hest, J. M. Luther, J. J. Berry and D. T. Moore, *Joule*, 2019, **3**, 2193-2204.
19. H. Gao, Q. Lu, K. Xiao, Q. Han, R. Lin, Z. Liu, H. Li, L. Li, X. Luo, Y. Gao, Y. Wang, J. Wen, Z. Zou, Y. Zhou and H. Tan, *Solar RRL*, 2021, **5**, 2100814.
20. B. Chen, Z. Yu, A. Onno, Z. Yu, S. Chen, J. Wang, Z. C. Holman and J. Huang, *Science Advances*, **8**, eadd0377.
21. Z. Yu, X. Chen, S. P. Harvey, Z. Ni, B. Chen, S. Chen, C. Yao, X. Xiao, S. Xu, G. Yang, Y. Yan, J. J. Berry, M. C. Beard and J. Huang, *Advanced Materials*, 2022, **34**, 2110351.
22. Z. Yu, J. Wang, B. Chen, M. A. Uddin, Z. Ni, G. Yang and J. Huang, *Advanced Materials*, 2022, **34**, 2205769.
23. J. Zhou, H. Qiu, T. Wen, Z. He, C. Zou, Y. Shi, L. Zhu, C.-C. Chen, G. Liu, S. Yang, F. Liu and Z. Yang, *Advanced Energy Materials*, 2023, **13**, 2300968.
24. J. Zhou, T. Wen, J. Sun, Z. Shi, C. Zou, Z. Shen, Y. Li, Y. Wang, Y. Lin, S. Yang, F. Liu and Z. Yang, *ACS Energy Letters*, 2024, **9**, 1984-1992.
25. J. Wang, Y. Pan, Z. Zhou, Q. Zhou, S. Liu, J. Zhang, C. Shi, R. Chen, Z. Zhao, Z. Cai, X. Qin, Z. Zhao, Z. Yang, Z. Liu and W. Chen, *Advanced Energy Materials*, 2024, **14**, 2402171.
26. X. Liao, X. Jia, W. Li, X. Lang, J. Zhang, X. Zhao, Y. Ji, Q. Du, C.-H. Kuan, Z. Ren, W. Huang, Y. Bai, K. Zhang, C. Xiao, Q. Lin, Y.-B. Cheng and J. Tong, *Nature Communications*, 2025, **16**, 1164.
27. J. Chen, J. Du, J. Cai, B. Ouyang, Z. Li, X. Wu, C. Tian, A. Sun, R. Zhuang, X. Wu, C. Chen, T. Cen, R. Li, T. Xue, Y. Zhao, K. Zhao, Q. Chen and C.-C. Chen, *ACS Energy Letters*, 2025, **10**, 1117-1128.